The Astrophysical Journal Letters, 901:L7 (9pp), 2020 September 20 https://doi.org/10.3847/2041-8213/abb3c5

Constraining the X-Ray–Infrared Spectral Index of Second-timescale Flares from SGR 1935+2154 with Palomar Gattini-IR

Kishalay De[1], Michael C. B. Ashley[2], Igor Andreoni[1], Mansi M. Kasliwal[1], Roberto Soria[3,4], Gokul P. Srinivasaragavan[1], Ce Cai[5,6], Alexander Delacroix[7], Tim Greffe[7], David Hale[7], Matthew J. Hankins[1], Chengkui Li[5], Daniel McKenna[7], Anna M. Moore[8], Eran O. Ofek[9], Roger M. Smith[7], Jamie Soon[8], Tony Travouillon[8], and Shuangnan Zhang[5,6]
[1] Cahill Center for Astrophysics, California Institute of Technology, 1200 E. California Boulevard, Pasadena, CA 91125, USA; kde@astro.caltech.edu
[2] School of Physics, University of New South Wales, Sydney, NSW 2052, Australia
[3] National Astronomical Observatories, Chinese Academy of Sciences, Beijing 100012, People's Republic of China
[4] Sydney Institute for Astronomy, The University of Sydney, Sydney, NSW 2006, Australia
[5] Key Laboratory of Particle Astrophysics, Institute of High Energy Physics, Chinese Academy of Sciences, 19B Yuquan Road, Beijing 100049, People's Republic of China
[6] University of Chinese Academy of Sciences, Chinese Academy of Sciences, Beijing 100049, People's Republic of China
[7] Caltech Optical Observatories, California Institute of Technology, Pasadena, CA 91125, USA
[8] Research School of Astronomy and Astrophysics, Australian National University, Canberra, ACT 2611, Australia
[9] Department of Particle Physics & Astrophysics, Weizmann Institute of Science, Rehovot 76100, Israel
Received 2020 July 4; revised 2020 August 24; accepted 2020 August 25; published 2020 September 18

Abstract

The Galactic magnetar SGR 1935+2154 has been reported to produce the first example of a bright millisecond-duration radio burst (FRB 200428) similar to the cosmological population of fast radio bursts (FRBs). The detection of a coincident bright X-ray burst represents the first observed multiwavelength counterpart of an FRB. However, the search for similar emission at optical wavelengths has been hampered by the high inferred extinction on the line of sight. Here, we present results from the first search for second-timescale emission from the source at near-infrared (NIR) wavelengths using the Palomar Gattini-IR observing system in the *J* band, enabled by a novel detector readout mode that allows short exposure times of ≈0.84 s with 99.9% observing efficiency. With a total observing time of ≈12 hr (≈47,728 images) during its 2020 outburst, we place median 3σ limits on the second-timescale NIR fluence of $\lesssim$18 Jy ms (13.1 AB mag). The corresponding extinction-corrected limit is $\lesssim$125 Jy ms for an estimated extinction of $A_J = 2.0$ mag. Our observations were sensitive enough to easily detect an NIR counterpart of FRB 200428 if the NIR emission falls on the same power law as observed across its radio to X-ray spectrum. We report nondetection limits from epochs of four simultaneous X-ray bursts detected by the Insight-HXMT and NuSTAR telescopes during our observations. These limits provide the most stringent constraints to date on fluence of flares at $\sim 10^{14}$ Hz, and constrain the fluence ratio of the NIR emission to coincident X-ray bursts to $R_{\rm NIR} \lesssim 0.025$ (fluence index $\gtrsim$0.35).

Unified Astronomy Thesaurus concepts: Radio transient sources (2008); Magnetars (992); Soft gamma-ray repeaters (1471)

Supporting material: data behind figure

1. Introduction

The source SGR 1935+2154 was discovered in 2014 as a short (≈0.2 s) burst (Stamatikos et al. 2014) by the Burst Alert Telescope on board the Neil Gehrels Swift Observatory (Gehrels et al. 2004). Subsequent follow-up in the X-ray wave bands revealed that the object was a new member of the class of soft gamma-ray repeaters (SGRs) originating from a Galactic magnetar with a spin period of ≈3.24 s, period derivative of $\dot{P} \approx 1.43 \times 10^{-11}$ s s^{-1}, characteristic age of ≈3600 yr, and surface magnetic field of $\sim 2 \times 10^{14}$ G (Israel et al. 2016). The source is coincident with the center of the supernova remnant G57.2+0.8 (Sun et al. 2011; Kozlova et al. 2016; Zhong et al. 2020; Zhou et al. 2020) at a distance of ≈10 kpc. For an assumed distance of 10 kpc, the energy released in the discovery burst was $\approx 3.6 \times 10^{37}$ erg in the observed energy range of 15–150 keV, based on a refined analysis of the burst spectrum reported in Lien et al. (2014). Pulsed radio emission has so far remained undetected at radio bands (Israel et al. 2016; Surnis et al. 2016; Younes et al. 2017; Lin et al. 2020b). In the optical and near-infrared (NIR) regime, a possible faint ($H \approx 24$ mag) counterpart has been identified in follow-up imaging with the Hubble Space Telescope (Levan et al. 2018).

Since its discovery, the source has sporadically gone into outburst over the past few years (Lin et al. 2020a), with the most recent being reported as a "forest" of X-ray bursts detected during 2020 April 27–28 (Palmer & Team 2020; Younes et al. 2020). Following the onset of the outburst, an unprecedented bright millisecond-duration radio burst (hereafter FRB 200428) was detected from the source by the Canadian Hydrogen Intensity Mapping Experiment (CHIME; The CHIME/FRB Collaboration et al. 2020) and STARE2 (Bochenek et al. 2020) telescopes, with an energy release that was ∼1000× brighter than any known radio burst from a Galactic source. The radio burst was accompanied by a bright hard X-ray counterpart detected by the INTEGRAL (Mereghetti et al. 2020), AGILE (Tavani et al. 2020), Konus-Wind (Ridnaia et al. 2020), and Insight Hard X-ray Modulation Telescope (HXMT; Li et al. 2020a) space telescopes. The large luminosity of the radio burst is only a factor of ≈40 smaller than that of the weakest extragalactic fast radio bursts (FRBs; Cordes & Chatterjee 2019; Petroff et al. 2019) observed at

cosmological distances to date, providing evidence that active SGRs could produce bright radio bursts akin to FRBs.

The simultaneous detection of the X-ray burst provides the first evidence of a multiwavelength counterpart for FRBs. Thus, several optical facilities performed follow-up observations of the source to detect and constrain the presence of optical counterparts coincident with radio/X-ray bursts (Niino et al. 2020; Lin et al. 2020b). However, the location of the source in the Galactic plane together with the high observed X-ray column density ($\sim 2 \times 10^{22}\,\mathrm{cm}^{-2}$; Israel et al. 2016; Younes et al. 2017; Li et al. 2020a) suggests a large line-of-sight optical extinction toward the source ($A_V \approx 7$–10 mag). In the case of FRB 200428, no optical counterpart was detected in a simultaneous observation by the BOOTES telescope (Lin et al. 2020b) to an extinction-corrected fluence limit of $\lesssim$4400 Jy ms. However, the inferred extinction in the NIR is substantially smaller, and expected to be ≈30% of the optical in the J band.

Palomar Gattini-IR (PGIR) is a new wide-field NIR time domain survey scanning the entire northern sky every two nights to a median depth of $J \approx 15.7$ AB mag (Moore & Kasliwal 2019; De et al. 2020a). With the implementation of a new detector readout mode that allows for fast (exposure time ≈0.84 s) and continuous (duty cycle ≈100%) exposures of the sky, we initiated targeted follow-up observations of the source. In this Letter, we describe the PGIR follow-up campaign and constraints from simultaneous NIR observations of SGR 1935+2154 at the times of detected X-ray bursts. Section 2 describes the observing strategy and resulting observation schedule. In Section 3, we describe the methods used to analyze the acquired data, and Section 4 uses the nondetection of NIR bursts to constrain the fluence ratios of multiwavelength counterparts of X-ray bursts from SGR 1935+2154. We conclude with a summary of our results and prospects for future searches in Section 5.

2. Observations

Following the detection of the train of X-ray bursts from SGR 1935+2154 (Palmer & Team 2020) and FRB 200428 (The CHIME/FRB Collaboration et al. 2020; Bochenek et al. 2020), we triggered targeted observations of the source using PGIR on UT 2020-05-01. Due to the short expected emission timescale for counterparts from X-ray/radio bursts from the source ($\lesssim$1 s) as well as the background noise limited nature of NIR imaging with this instrument (see Table 1 in De et al. 2020a), we used the shortest possible exposure time allowed by the standard readout scheme (1.65 s) used in survey operations with an observing efficiency of 30% including dithers. Following this initial epoch, we significantly increased our observing efficiency, as well as our sensitivity to short timescale flares, by using a newly implemented readout mode of the H2RG detector array in Palomar Gattini-IR (De et al. 2020a). In this new mode, the detector is read out and digitized continuously while exposing on the sky, with an effective exposure time equivalent to the frame readout time of ≈0.84 s (see Appendix A for details).

Table 1 provides a summary of all the observing epochs on the source, including the readout mode used and the placement of the source in the large field of view. While the initial observations were designed to monitor the source for the total duration of its night time visibility from Palomar (≈4.5 hr below airmass of 2) near the peak of its outburst, subsequent epochs in the second half of 2020 May were coordinated with the published visibility windows of the source with the Insight-HXMT satellite[10] and the CHIME telescope (K. Smith, 2020, personal communication).

3. Data Analysis

The location of the source in a dense region of the Galactic plane together with the large pixel scale and undersampled point-spread functions (PSFs) of the Gattini observing system present several challenges to the data reduction procedure, which were modified and adapted from the nominal survey mode. Appendix B provides a detailed summary of the reduction process adopted for this data set. Figure 1 shows an example triplet of a fast readout science frame centered at the location of the source, the corresponding reference image and the resulting difference image. We were able to obtain high-quality difference images in all the epochs, which show only background noise fluctuations and residual astrometric/Poisson noise from nearby bright stars.

Figure 2 shows a time series of the measured difference flux during one of the observing sessions.[11] In order to estimate the uncertainty and signal-to-noise ratio of the flux measurements, we measured the standard deviation of the fluxes in a running window of 200 observations around each image in the sequence. The measured flux scatter exceeds the propagated noise terms by ≈10% due to the presence of unaccounted noise terms such as correlated noise between the pixels introduced during the resampling process. The measured flux uncertainty exhibits temporal variations of the order of ≈20% over the duration of the night, reflecting the variation in the foreground J-band sky brightness.

In addition to random scatter introduced due to time variable airglow in the J-band sky, the measured fluxes also show slow temporal variations (over timescales of tens of minutes) in the median (see Figure 2) that correlate with the changing scatter from the sky background, thus arising from imperfect background subtraction with the changing sky background. Since this effect introduces a slow temporal trend, we subtract it using a running median around each image since we aim to detect short timescale flares ($\sim$1 s) from the source. The resulting residual time series is shown in Figure 2, and is consistent with Gaussian noise in the flux measurements.

4. Results

Correlated variability between X-ray and NIR emission has been detected in several known Galactic magnetars, but over timescales of days to years (e.g., Rea et al. 2004; Tam et al. 2004; Israel et al. 2005). Fast optical flaring over timescales of a few seconds has also been observed in a candidate Galactic soft gamma-ray repeater (Castro-Tirado et al. 2008; Stefanescu et al. 2008). In the case of SGR 1935+2154, a probable faint NIR counterpart (at $H \approx 24$ mag) was identified with a deep Hubble Space Telescope exposure during its 2015–2016 outbursts (Levan et al. 2018), where the IR emission was shown to be enhanced during periods of the X-ray outburst. However, it was suggested that the lack of a direct correlation between the NIR—X-ray fluxes disfavors a disk-reprocessing

[10] Published at http://enghxmt.ihep.ac.cn/dqjh.jhtml.

[11] The measured flux in counts was converted to mJy using the *2MASS* zero-points published at https://old.ipac.caltech.edu/2mass/releases/allsky/doc/sec6_4a.html. The corresponding $J = 0$ flux density is 1594 Jy.

Table 1
Summary of Observing Sessions of SGR 1935+2154 with PGIR

ID	UT Start	UT End	Mode	Exp. Time (s)	N	Total Exposure (s)	Duty Cycle (%)	3σ Limit (mJy/Jy ms)
1	2020-05-01 08:24:38.9	2020-05-01 12:34:53.6	I	1.65	2722	4491.3	29.9	9/16
2*	2020-05-02 07:49:45.5	2020-05-02 12:34:14.1	II	0.84	18009	15127.6	89.7	25/21
3*	2020-05-05 08:20:13.7	2020-05-05 12:31:09.0	II	0.84	15917	13370.3	89.7	23/19
4	2020-05-23 11:23:09.0	2020-05-23 11:38:27.3	III	0.84	1084	910.6	99.9	16/13
5	2020-05-24 06:57:05.3	2020-05-24 07:29:43.4	III	0.84	2310	1940.4	99.9	19/16
6†	2020-05-24 11:09:27.4	2020-05-24 11:34:12.3	III	0.84	1706	1433.0	97.3	21/18
7	2020-05-28 06:13:49.2	2020-05-28 07:13:34.7	III	0.84	4229	3552.4	99.9	18/15
8†	2020-05-31 09:01:30.0	2020-05-31 09:39:32.9	III	0.84	1751	1470.8	64.6	62/52

Note. The Mode column refers to the observing configuration of the system during the respective epoch. Mode I indicates the use of the standard observing mode of the survey including dithers between exposures and lower observing efficiency. Mode II indicates the fast readout mode discussed in the text. Both Modes I and II had the telescope aligned to the default observing grid and the source placed away from the best focused part of the field (see the discussion of PSF variation in De et al. 2020a). Mode III indicates the fast readout mode with the source placed in the best focused part of the detector leading to better sensitivity. N denotes the number of images that produced good-quality subtractions in the session. The duty cycle is a conservative lower limit for the first pixel read out in each detector channel. The limiting flux denotes the median limiting flux in the individual exposures at the location of the source as measured from the observed scatter of fluxes in the difference image. Data acquired during epochs marked by * were affected by a bug in the readout that repeated every 10th exposure in the sequence (i.e., every 9th and 10th exposure were identical), leading to reduced duty cycle. Epochs marked by † were affected by intermittent clouds leading to reduced observing duty cycle.

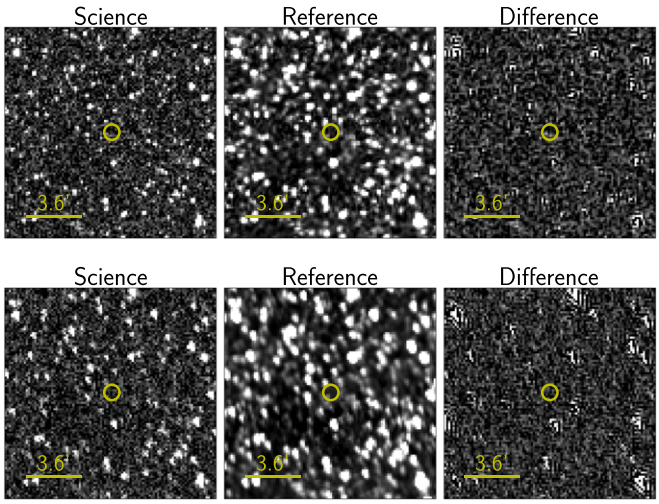

Figure 1. Example cutouts of a science (left column), reference (middle column), and difference image (right column) acquired in our observing sequence. North is up and east is left in each panel. The top and bottom rows show examples of the subtractions with the source placed in different parts of the focal plane with differing PSFs—the top row shows the case where the source was placed in the best part of the detector with approximately symmetric PSFs, while the lower row shows the same in a poorer region of the focal plane with elongated PSFs. In both cases, the difference image produced using ZOGY (Zackay et al. 2016) only shows residual astrometric and Poisson noise from nearby bright stars, with no statistically significant transient emission detected at the location of SGR 1935+2154 (yellow circle).

scenario for the NIR emission, and was likely more consistent with a magnetospheric origin of both the emission components (Levan et al. 2018). Here, we focus instead on the detection and limits on second-timescale flares in the NIR, which remain so far observationally unconstrained from this source.

Over the duration of ≈12 hr of observations (Table 1), we identified no reliable detections in the NIR time series at a flux level above $3\,\sigma$ from the background noise, beyond that expected from Gaussian noise. The median observed 3σ fluence limit on NIR bursts is ≈20 Jy ms (uncorrected for line-of-sight extinction). In order to constrain potential multi-wavelength counterparts, we searched all available public reports of X-ray and radio bursts from the source within our observing time intervals. A total of four X-ray bursts were reported by the HXMT (Li et al. 2020b)[12] and NuSTAR (Borghese et al. 2020) satellites during our observations. Table 2 provides an overview of the X-ray bursts reported during our observations. Notably, no significant emission was found detected around the reported epochs of four X-ray bursts. Below, we use the derived limits from our observations to constrain the fluence ratio of NIR bursts when compared to both the coincident X-ray bursts as well as the observed X-ray to radio spectrum of FRB 200428.

4.1. Extinction along the Line of Sight

Israel et al. (2016) find the neutral hydrogen column density ($n_{\rm H}$) along the line of sight to be $n_{\rm H} = (1.6 \pm 0.2) \times 10^{22}\,{\rm cm}^{-2}$ using XMM-Newton spectra fitted by a two-component power-law (PL) and blackbody model, from which we obtain an attenuation $A_V = 7.2 \pm 0.9$ mag (Güver & Özel 2009) and $A_J = 2.0 \pm 0.3$ mag (Rieke & Lebofsky 1985). This extinction value is consistent with $1.82 < A_J < 1.97$ mag obtained using 3D dust map based on Pan-STARRS 1, Gaia, and 2MASS optical/NIR data (Green et al. 2019) assuming a distance of 8–12 kpc, although these dust maps suffer the lack of bright M-dwarf stars observable at these distances. For $A_J = 2.0 \pm 0.3$ mag, the corresponding median limits on the intrinsic fluence of the bursts will be ≈85–150 Jy ms (within a factor of 2). For the rest of this work, we assume an extinction of $A_J = 2.0$ mag toward the source, noting that the exact value does not significantly affect our constraints below due to the smaller effect of extinction in the NIR.

4.2. Constraints on the NIR Fluence Ratio from Coincident X-Ray Bursts

In Table 2, we list the X-ray bursts reported from HXMT and NuSTAR during our observing sequence, together with the reported X-ray fluences from HXMT and our measured difference image flux and corresponding 3σ limit on the NIR

[12] The updated list of bursts are available at http://enghxmt.ihep.ac.cn/bfy/331.jhtml.

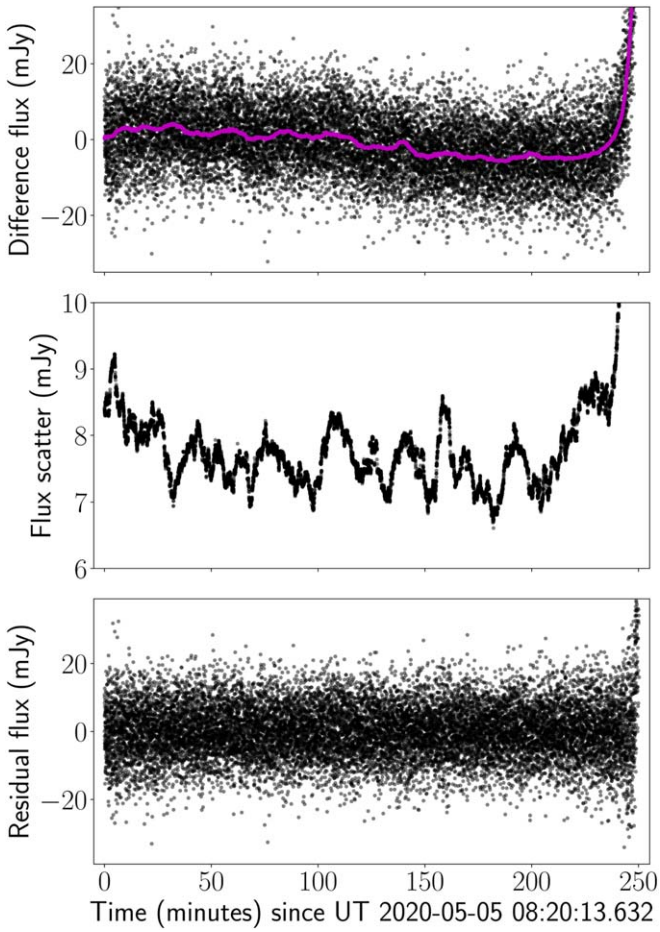

Figure 2. Example of the method used to search for second-timescale emission from SGR 1935+2154 using Gattini-IR data taken on UT 2020-05-05. (Top panel) Forced photometry time series of fluxes measured at the location of the source in the difference images, with each dot representing a single image and the magneta lines representing a running median of fluxes measured in a window of 200 images in each side. The large increase in the background at the end of the observation is due to the approach of 12° twilight at the end of the observation. (Middle panel) Measured standard deviation in fluxes at the location of the source using the same window size as in the running median of the top panel. Noise variations due to the time variable airglow in the *J* band are clearly visible. (Bottom panel) Residual flux obtained from subtracting the longer timescale airglow variations (shown in magneta in the top panel) from the observed flux.

(The data used to create this figure are available.)

fluence.[13] We note that the expected dispersion delay between X-ray and optical pulses for the reported DM of ≈330 pc cm^{-3} (Bochenek et al. 2020; The CHIME/FRB Collaboration et al. 2020; Zhang et al. 2020) is $\sim 10^{-11}$ s and thus not important for our observations. However, since a delay between the X-ray and optical emission could arise as a result of the intrinsic emission mechanism, we show in Figure 3 the measured difference flux in a window of ≈6 minutes centered on the times of the reported X-ray bursts[14]

[13] In order to be consistent with reported X-ray bursts, we define fluence as $\mathcal{F} = \nu f_\nu \delta t$, where ν is the observed frequency, f_ν is the spectral flux density, and δt is the exposure time for our data.

[14] For comparison, we note that the X-ray and radio emission observed in FRB 200428 was coincident within a maximum conservative uncertainty of ≈0.5 s, and shorter than our exposure time.

No significant emission is identified within this time window of the reported X-ray bursts, and we list the derived limits on the NIR fluence of the bursts in Table 2. Combining the *J*-band flux limits from the epochs of the four X-ray bursts, we obtain a 3σ limit on the NIR fluence of 2.9×10^{-11} erg cm^{-2}. However, we caution that these bursts exhibit diversity in their X-ray spectral characteristics and hence their NIR fluence ratios may not be derived from the same population. The strongest simultaneous constraint on the NIR to X-ray fluence ratio ($R_{\rm NIR}$) is derived from the brightest burst (Burst B), where the nondetection of NIR emission constrains $R_{\rm NIR} \lesssim 2.5 \times 10^{-2}$ after correcting for extinction. For comparison, we note that the extinction-corrected $R_{\rm NIR}$ for longer-term correlated X-ray–NIR outbursts (over ∼days—weeks) observed in Galactic magnetars range from typical values of $\sim 10^{-4}$ (as seen for SGR 1935+2154 as well as some other X-ray pulsars; Rea et al. 2004; Tam et al. 2004; Levan et al. 2018) to $\sim 10^{-2}$ (for the IR counterpart of SGR 1806-20; Israel et al. 2005).

4.3. Comparison to the Multiwavelength Properties of FRB 200428

As the only other X-ray burst from SGR 1935+2154 that has been reported with a multiwavelength (radio) counterpart, we compare the NIR limits to the observed spectral energy distribution (SED) of FRB 200428. The striking time coincidence between two X-ray pulses observed in the X-ray burst associated with FRB 200428 (Li et al. 2020a; Mereghetti et al. 2020) with the two radio pulses detected by CHIME (The CHIME/FRB Collaboration et al. 2020) potentially suggests a common emission source extending from the X-ray to radio frequencies. Li et al. (2020a) show that the HXMT X-ray burst associated FRB 200428 was characterized with a hard power-law spectrum with a photon index of $\Gamma \approx 1.5$, corresponding to a flux density dependence of $f_\nu \propto \nu^{-0.5}$ and fluence dependence of $\mathcal{F} \propto \nu^{0.5}$. In particular, they show that the observed STARE2 fluence at ∼1.4 GHz can be explained by a single power law in f_ν extending from X-ray to radio frequencies (see also Ridnaia et al. 2020).

In Figure 4, we show the observed fluence of FRB 200428 as a function of frequency, which suggests a fluence dependence of approximately $\mathcal{F} \propto \nu^{0.46}$. In addition, Figure 4 shows the observed fluences of the X-ray bursts reported within our observing session along with our NIR fluence limits. While the spectrum of the X-ray burst for FRB 200428 remains unconstrained below ∼1 keV, Figure 4 shows that our observations had the sensitivity to detect (at $\sim 30\sigma$ confidence) an NIR counterpart of FRB 200428 if PGIR was observing at the time of the burst and the emission was characterized by a continuous power law extending from X-ray to radio frequencies. We note that the BOOTES limit from Lin et al. (2020b) does not rule this out. However, we caution that the observed radio spectrum of FRB 200428 shows signatures of narrow bandwidth fluctuations (The CHIME/FRB Collaboration et al. 2020; Bochenek et al. 2020). Hence, the SED of FRB 200428 may not be consistent with a single power law extending from X-ray to radio frequencies, although propagation effects may affect this interpretation.

We compare this fluence index (β) to the expected NIR emission from the coincident X-ray bursts within our observing sessions. Here we refer to the fluence index as the exponential factor β of the observed fluence that scales as $\mathcal{F} \propto \nu^\beta$. The strongest constraints on the fluence index are derived from the

Table 2
List of X-Ray Bursts Reported by High-energy Instruments within the Gattini-IR Observing Sequences

ID	Instrument	Trigger Time (UT)	Duration (s)	X-Ray Fluence (erg cm^{-2})	Obs Start (UT Day)	Obs End (UT Day)	Diff. Fluence (erg cm^{-2})	3σ Limit (erg cm^{-2})
A	HXMT/NuSTAR	2020-05-02 10:17:26.00	0.076	7.56×10^{-9}	10:17:25.90	10:17:26.74	2.69×10^{-12}	4.93×10^{-11}
B†	HXMT/NuSTAR	2020-05-02 10:25:25.80	0.415	1.76×10^{-8}	10:25:25.07	10:25:26.77	-3.64×10^{-11}	6.49×10^{-11}
C	HXMT	2020-05-02 10:46:20.85	0.077	1.16×10^{-10}	10:46:20.12	10:46:20.96	-7.64×10^{-12}	5.14×10^{-11}
D†	HXMT	2020-05-05 12:09:29.75	0.039	7.97×10^{-9}	12:09:28.94	12:09:30.65	-1.81×10^{-11}	7.73×10^{-11}

Note. The Fluence column denotes the fluence reported by the HXMT satellite, while the duration denotes their T_{90} measurement. The Obs Start and Obs End columns denote the start and end of the exposure that contained the trigger time of the X-ray burst, with respect to the start of the UT day (00:00:00). The Diff. Fluence and 3σ Limit columns denote the IR fluence computed from the difference flux and the corresponding 3σ limit. For bursts denoted by †, the duration of the burst was covered by two consecutive and continuous exposures in the sequence, in which case we reported a weighted flux measurement between the two exposures and its corresponding uncertainty. The IR flux measurements have not yet been corrected for extinction since that is model dependent.

brightest burst (burst B), for which the fluence index is constrained to $\beta > 0.35$. The corresponding constraint on the spectral index α of f_ν is $\alpha > -0.65$. The derived limit on the fluence index is not constraining enough to rule out an NIR counterpart for these X-ray bursts with the same spectral behavior as that of FRB 200428, although it is within a factor of ≈1.5 from the estimated fluence index of FRB 200428. The nondetection is consistent with radio constraints derived from the nondetection of radio bursts by FAST of 29 bursts from SGR 1935+2154 detected by Fermi-GBM (Lin et al. 2020b), who derive deep limits of ∼0.03 Jy ms at 1.25 GHz for these bursts. These nondetections require much steeper X-ray to radio fluence indices ($\beta > 1.2$) for the majority of bursts from SGR 1935+2154, suggesting that our limits in the NIR would not be deep enough to detect possible counterparts of the majority of bursts.

4.4. Comparison to Theoretical Models

Recent works have aimed to constrain several proposed models for FRBs to explain the observed occurrence of FRB 200428 simultaneously with the bright X-ray burst (e.g., Lu et al. 2020; Margalit et al. 2020). These models primarily revolve around two scenarios—one where the X-ray/radio emission is generated inside the neutron star magnetosphere via coherent curvature radiation (e.g., Pen & Connor 2015; Cordes & Wasserman 2016; Kumar et al. 2017; Lu & Kumar 2018) or via coherent maser processes produced at shock interaction of relativistic ejecta with circumstellar material (e.g., Lyubarsky 2014; Beloborodov 2020; Metzger et al. 2019; Margalit et al. 2020). In particular, the X-ray, optical/NIR, and radio emission may not be generated at the same location near the neutron star in several of these scenarios. Since the theoretical predictions for multiwavelength counterparts are not well constrained enough to interpret our upper limits directly, we only briefly compare them to our NIR observational data.

Chen et al. (2020) provide a summary of the predictions for the fluence in the aforementioned models. In the case of the relativistic shock interaction model by Beloborodov (2020), if the the blast wave strikes a wind bubble in the tail of a previous flare, a bright optical flare could result with an optical to radio fluence ratio of $\mathcal{F}_{\rm opt}/\mathcal{F}_{\rm radio} \lesssim 10^5$ (Chen et al. 2020). If some X-ray bursts from SGR 1935+2154 during the PGIR campaign were accompanied by a radio burst similar to FRB 200428, then we have the corresponding prediction of $R_{\rm NIR} \lesssim 0.1$ for $\mathcal{F}_{\rm radio}/\mathcal{F}_{\rm X-ray} \sim 10^{-6}$ (as observed by STARE2; Bochenek et al. 2020) and $R_{\rm NIR} \lesssim 0.01$ for $\mathcal{F}_{\rm radio}/\mathcal{F}_{\rm X-ray} \sim 10^{-7}$ (as observed by CHIME; The CHIME/FRB Collaboration et al. 2020). Our upper limits are thus comparable to these model predictions for the brighter X-ray bursts. On the other hand, for the curvature radiation model of Lu & Kumar (2018), the NIR/optical (or higher-frequency) emission from the coherently emitting particles is expected to be very faint. The transient event may be accompanied by incoherent emission processes inside the magnetosphere, and the maximum possible NIR flux from any incoherent emission processes from an emitting volume of radius $r = 10^8 r_8$ cm and plasma temperature $T = 10^8 T_8$ K is given by

$$\mathcal{F}_{\rm max} \sim (h\nu/kT)^3 \sigma T^4 (r/D)^2, \quad (1)$$

$$\sim 10^{-13} T_8 r_8^2 \text{ erg cm}^{-2} \text{ s}^{-1}, \quad (2)$$

where $D \sim 9$ kpc is the distance to the source. We see that the NIR/optical emission from within the magnetosphere is undetectable in our observations for burst duration $\lesssim$1 s.

5. Summary

In this Letter, we have presented results from a targeted follow-up campaign to search for second-timescale NIR flares from the Galactic magnetar SGR 1935+2154 using Palomar Gattini-IR. The observations were enabled with a recently implemented detector readout mode that allows for high time resolution readout of the detector array with nearly 100% observing efficiency. We found no significant counterparts for second-timescale flares from the source above a median 3σ fluence limit of ≈20 Jy ms. This nondetection, together with the relatively low inferred extinction toward the source at NIR wavelengths ($A_J \approx 2.0 \pm 0.3$ mag) allows us to place the most stringent extinction-corrected constraints to date on second-timescale flares from the source of ≈85–150 Jy ms at optical/NIR wavelengths ($\nu \sim 10^{14}$ Hz). The NIR limit corresponds to an energy $E \lesssim 3 \times 10^{36}$ erg at a distance of 9 kpc (Zhong et al. 2020), and is within an order of magnitude of that reported in the radio for FRB 200428 at 1.25 GHz (≈2×10^{35} erg; Bochenek et al. 2020). It is also several orders of magnitude deeper than reported optical limits from nearby well-localized FRBs (∼10^{43-46} erg; Hardy et al. 2017; Andreoni et al. 2020).

A total of four X-ray bursts were detected by the HXMT and NuSTAR telescopes within our continuous observing campaign, although no NIR counterparts were detected. The nondetection of NIR emission around these bursts constrain the NIR to X-ray fluence ratio to $R_{\rm NIR} \lesssim 2.5 \times 10^{-2}$. Comparing these fluence limits to the radio/X-ray fluence observed in FRB 200428, we show that our observations were sensitive enough to detect an NIR counterpart at a significance

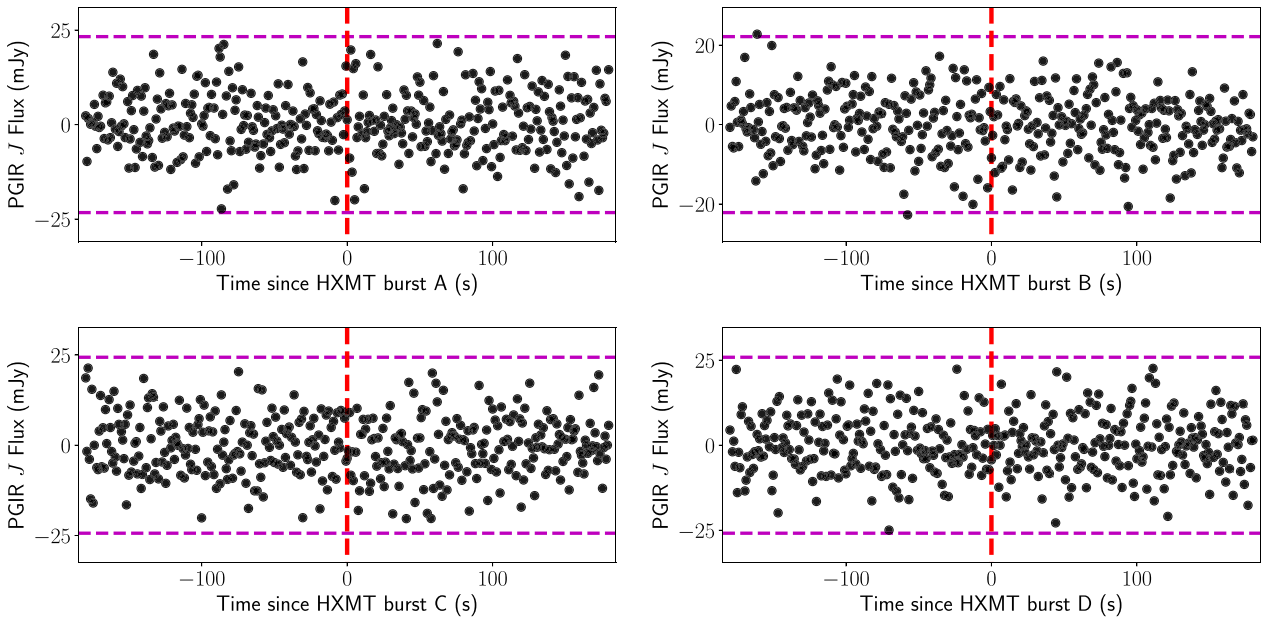

Figure 3. Time series of difference flux measurements over 360 s intervals centered on the times of known X-ray bursts listed in Table 2. The burst numbering indicated are the same as those in Table 2. The red vertical line shows the time of the reported burst, while the magneta horizontal dashed lines show the 3σ noise levels around the time of observation. No significant emission is detected at the 3σ level around the reported times of the X-ray bursts.

of ∼30σ if PGIR was observing at the time of FRB 200428 and the NIR emission falls on the same power law suggested for the radio/X-ray emission. The nondetection of NIR emission associated with the brightest X-ray burst within our observation time constrains the X-ray to NIR fluence index of the burst to be $\beta > 0.35$ (spectral index $\alpha > -0.65$).

As Palomar Gattini-IR performs the first all-sky untargeted time domain survey of the dynamic infrared sky at timescales of days to years over the survey duration, these observations further demonstrate a unique new capability of this instrument to probe the infrared time domain sky at second timescales. Although the instrument uses a small (30 cm) telescope with coarse pixels that severely limit its sensitivity due to the bright *J*-band foreground, these observations prove the scientific utility of specialized NIR detector readout modes in finding large-amplitude second-timescale flares from dust-obscured sources in the Galactic plane. This advocates for a systematic exploration of this hitherto unexplored phase space, which is possible with PGIR not only for single sources (as demonstrated in this work) but for large patches of the sky, enabled by the instrument's large field of view.

We thank the Insight/HXMT team for their kind cooperation in coordinating observations and quickly providing fluence estimates. We thank K. Smith for cooperation regarding the CHIME observability windows. We thank C. Bochenek, W. Lu, V. Ravi, and S. R. Kulkarni for valuable discussions on this work.

Palomar Gattini-IR (PGIR) is generously funded by Caltech, Australian National University, the Mt Cuba Foundation, the Heising Simons Foundation, the Bi-national Science Foundation. PGIR is a collaborative project among Caltech, Australian National University, University of New South Wales, Columbia University and the Weizmann Institute of Science. This work was supported by the GROWTH (Global Relay of Observatories Watching Transients Happen) project funded by the National Science Foundation under PIRE grant No 1545949. GROWTH is a collaborative project among the California Institute of Technology (USA), University of Maryland College Park (USA), University of Wisconsin Milwaukee (USA), Texas Tech University (USA), San Diego State University (USA), University of Washington (USA), Los Alamos National Laboratory (USA), Tokyo Institute of Technology (Japan), National Central University (Taiwan), Indian Institute of Astrophysics (India), Indian Institute of Technology Bombay (India), Weizmann Institute of Science (Israel), The Oskar Klein Centre at Stockholm University (Sweden), Humboldt University (Germany), Liverpool John Moores University (UK), and University of Sydney (Australia).

Appendix A
Fast Readout Mode

Conventional readout in the H2RG array requires one frame scan to reset and measure the resulting initial offset (including random errors) and a second frame to measure the final value (Figure 5, top). The signal is then the difference of these two frames. At the fastest frame rate (with no delay between frames), the duty cycle drops to 50%. To address this deficiency, we altered the readout sequence such that immediately after the signal in a given line is read out, the line is reset and the baseline for the next frame is digitized before preceding to the next line (Figure 5, bottom). Signal is then being recorded except during the interval between signal and post-reset level samples, i.e., dead time has been reduced from the time to scan through the entire frame to the time to read just one line.

Given the high sky noise, we were able to reduce signal sampling time so that pixel time was reduced from typical ≈6–7 μs to 3.1 μs. With two samples per pixel per frame, the frame time is then 0.848039 s. The dead time between reading the final sample and the next post-reset sample ≈200 μs. The first exposure in a sequence still requires two frames, with the

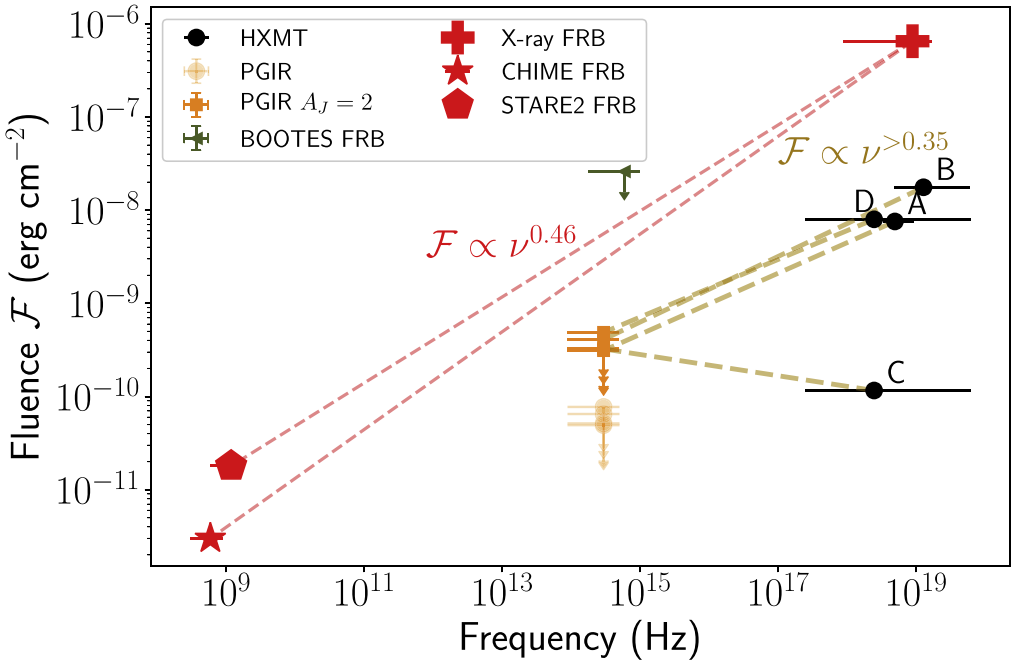

Figure 4. Constraints on the NIR fluence of X-ray bursts from SGR 1935+2154 based on limits from Palomar Gattini-IR. For comparison, we show the observed X-ray and radio fluence of FRB 200428 (in red) detected by CHIME and STARE2 in coincidence with a hard X-ray burst detected by HXMT, INTEGRAL, AGILE, and Konus-Wind. Optical limit from the BOOTES telescope for FRB 200428 is also shown. Limits from the PGIR campaign are shown in orange, with transparent circles showing raw limits, while solid squares show extinction-corrected limits for $A_J = 2.0$ mag. The four X-ray bursts detected by HXMT and NuSTAR during the PGIR observing sessions (labels indicated as per Table 2) are shown with yellow dashed lines connecting the corresponding NIR limits. For each X-ray burst, we place the fluence at the frequency corresponding to the peak of the fluence spectrum ($=\nu f_\nu$) observed in the X-rays (and its uncertainty). The estimated fluence peaks for bursts A and B are consistent with the observed spectrum of the bursts from NuSTAR observations (Borghese et al. 2020), where the fluence is observed to rise up to at least ~20 keV. In the case of bursts C and D, the fluence spectrum was not well constrained, and hence they are placed nominally at 10 keV with error bars spanning the full HXMT sensitivity range. The observed fluence index for FRB 200428 and constraints derived for the X-ray bursts are shown.

first frame establishing the post-reset level. The duty cycle for an N frame sequence is then

$$\frac{N-1}{N} \times \frac{0.848039 - 0.0002}{0.848039}, \tag{A1}$$

which approaches 99.98% for long exposure sequences. Anomalous behavior due to self-heating variations were avoided by clocking the detector continuously. The camera was setup to read continuously and store data in a 10 frame circular buffer in the computer's memory with the only distinction between idling and exposing being whether the data was written to disk.

Appendix B
Data Reduction

While the nominal survey mode operations in Gattini-IR use the `Drizzle` (Fruchter & Hook 2002) technique to reconstruct the undersampled PSFs by stacking several dithered images taken on sky, our requirement for high time resolution at the native image readout timescale makes it unsuitable for this application. We thus modified our default data processing pipeline to perform detrending, astrometry, photometry, and subtractions on individual images at the native pixel scale of the detector, which we describe below.

B.1. Flat-field Generation and Image Detrending

A master flat-field was created for the readout mode using a median combination of 400 sky images across several observing nights in order to calibrate the pixel-to-pixel response of the array in the new readout mode. Using images acquired over a wide range of times ensures that temporal structures in the sky background variation do not affect the resulting flat-field. Each acquired image (2048 × 2048 pixels) was flat-fielded using the derived flat-field, and only 1/16 of the full image (512 × 512 pixels; hereafter referred to as a subquadrant as per the terminology in De et al. 2020a) containing the target of interest was retained for further processing. Retaining a smaller portion of the image containing the source leads to a large reduction in the variation of the PSF across the image, thus producing better-quality astrometric and photometric solutions, as well as subtractions downstream.

B.2. Astrometry, Photometry, and Reference Image Generation

An astrometric and photometric solution for the subquadrant was derived using relatively bright and isolated stars in the field. The calibration was performed using the same techniques as in the regular Gattini observing system and using the same reference catalog, which is calibrated astrometrically to Gaia DR2 and photometrically to the 2MASS point source catalog. The astrometric solutions achieved typical rms of ≈1.0–1.″2 (≲1/8 of a pixel), while the photometric solutions have typical uncertainties on the zero-point of ≈1% as calibrated from ~100 stars in each image.

Due to the location of the source in a dense region of the Galactic plane (see Figure 1) and the highly nonstationary background limited by confusion noise, direct aperture photometry measurements on unsubtracted images are not well suited for deriving accurate constraints on the source flux. We thus created for each observing night, a deep median stack of

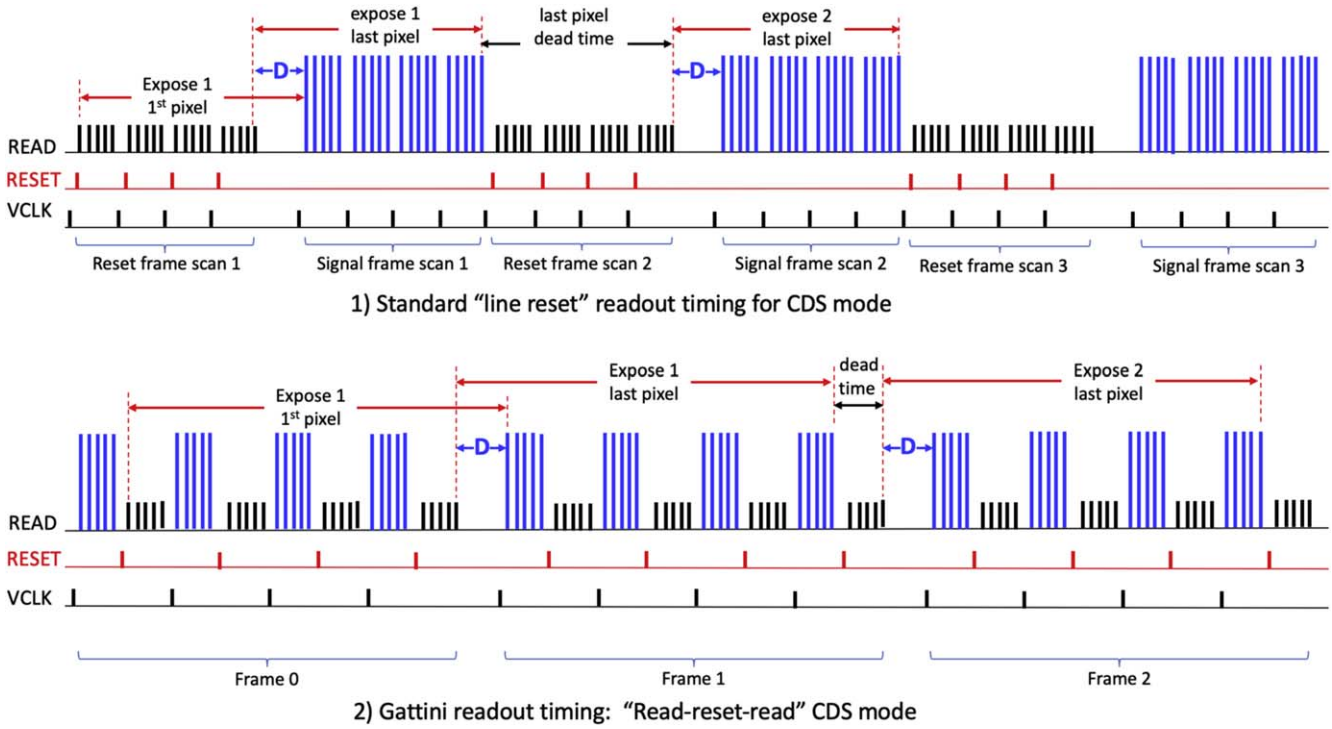

Figure 5. Difference between a conventional H2RG readout scheme and the readout technique used in the new continuous fast readout mode of the H2RG array in PGIR. In each panel, we show the time sequence of pixel reset and signal readout for a hypothetical detector of 20 pixels (4 rows with 5 pixels per row). Three horizontal lines in each panel indicate the reset and readout sequence. The top horizontal line in each panel (labeled as READ) shows progression of the pixel readout in each row, with short black vertical lines showing a post-reset pixel readout, and long blue vertical lines showing a post-expose pixel signal readout (the sky signal is thus the difference between these two values). Red vertical lines on the second horizontal line (labeled as RESET) mark the time of reset for each row of pixels, while black vertical lines on the third horizontal line (labeled as VCLK) mark the start time of signal readout for each row. In the top panel, the timing of pixel reads, reset, and vertical clock for conventional correlated double sampling (CDS) is shown, where each row is reset then digitized to establish a baseline. All baseline samples are acquired before reading the frame again to record signal levels. Light falling on the detector between reading signal of one exposure and the baseline of the next is not recorded, resulting in only 50% exposure duty cycle when exposure delay (D) is set to zero for continuous readout. In the bottom panel, we show the PGIR fast readout mode, where the signal is read, then the row is reset, and baseline samples are acquired before advancing to the next row. Dead time is thus reduced from a full frame scan time to the time to read one row. The signal samples in the first frame of a sequence and the baseline samples in the last are discarded.

400 subquadrants to serve as a reference image with nearly identical PSF as the science images taken each night. Since the reference stack was produced as a median combination as implemented in `Swarp` (Bertin et al. 2002; at the same pixel scale as that of the science images), we do not expect any short timescale emission to contaminate the reference image.

B.3. Difference Imaging and Forced Photometry

Each reduced subquadrant was processed through image subtraction by resampling the respective reference image (one for each night) to the coordinate grid of the science frame. The resampled reference frame was then flux-scaled to each science frame using common cross-matched stars in the two images. The typical astrometric registration uncertainty between the cross-matched stars was $\approx$0.1–0.15 pixels, while the corresponding flux-scaling certainty was $\lesssim$5%. Image subtraction was performed using the ZOGY algorithm (Zackay et al. 2016), including propagation of noise uncertainties from the science and reference images to produce an uncertainty image for each produced difference image (as in De et al. 2020b). The flux and its uncertainty at the location of the source were measured directly from the difference images by performing a weighted flux measurement using the difference image PSF at the location of the target in the difference image and the corresponding uncertainty image.

ORCID iDs

Kishalay De https://orcid.org/0000-0002-8989-0542
Igor Andreoni https://orcid.org/0000-0002-8977-1498
Mansi M. Kasliwal https://orcid.org/0000-0002-5619-4938
Roberto Soria https://orcid.org/0000-0002-4622-796X
Matthew J. Hankins https://orcid.org/0000-0001-9315-8437
Eran O. Ofek https://orcid.org/0000-0002-6786-8774

References

Andreoni, I., Lu, W., Smith, R. M., et al. 2020, ApJL, 896, L2
Beloborodov, A. M. 2020, ApJ, 896, 142
Bertin, E., Mellier, Y., Radovich, M., et al. 2002, in ASP Conf. Ser. 281, Astronomical Data Analysis Software and Systems XI, ed. D. A. Bohlender, D. Durand, & T. H. Handley (San Francisco, CA: ASP), 228
Bochenek, C. D., Ravi, V., Belov, K. V., et al. 2020, arXiv:2005.10828
Borghese, A., Coti Zelati, F., Rea, N., et al. 2020, arXiv:2006.00215
Castro-Tirado, A. J., de Ugarte Postigo, A., Gorosabel, J., et al. 2008, Natur, 455, 506
Chen, G., Ravi, V., & Lu, W. 2020, ApJ, 897, 146
Cordes, J. M., & Chatterjee, S. 2019, ARA&A, 57, 417
Cordes, J. M., & Wasserman, I. 2016, MNRAS, 457, 232
De, K., Hankins, M. J., Kasliwal, M. M., et al. 2020a, PASP, 132, 025001
De, K., Kasliwal, M. M., Tzanidakis, A., et al. 2020b, arXiv:2004.09029
Fruchter, A. S., & Hook, R. N. 2002, PASP, 114, 144
Gehrels, N., Chincarini, G., Giommi, P., et al. 2004, ApJ, 611, 1005
Green, G. M., Schlafly, E., Zucker, C., Speagle, J. S., & Finkbeiner, D. 2019, ApJ, 887, 93
Güver, T., & Özel, F. 2009, MNRAS, 400, 2050

Hardy, L. K., Dhillon, V. S., Spitler, L. G., et al. 2017, MNRAS, 472, 2800
Israel, G., Covino, S., Mignani, R., et al. 2005, A&A, 438, L1
Israel, G. L., Esposito, P., Rea, N., et al. 2016, MNRAS, 457, 3448
Kozlova, A. V., Israel, G. L., Svinkin, D. S., et al. 2016, MNRAS, 460, 2008
Kumar, P., Lu, W., & Bhattacharya, M. 2017, MNRAS, 468, 2726
Levan, A., Kouveliotou, C., & Fruchter, A. 2018, ApJ, 854, 161
Li, C. K., Lin, L., Xiong, S. L., et al. 2020a, arXiv:2005.11071
Li, C. K., Cai, C., Zhang, S. N., et al. 2020b, GCN, 28027, 1
Lien, A. Y., Barthelmy, S. D., Baumgartner, W. H., et al. 2014, GCN, 16522, 1
Lin, L., Göğüş, E., Roberts, O. J., et al. 2020a, ApJ, 893, 156
Lin, L., Zhang, C. F., Wang, P., et al. 2020b, arXiv:2005.11479
Lu, W., & Kumar, P. 2018, MNRAS, 477, 2470
Lu, W., Kumar, P., & Zhang, B. 2020, arXiv:2005.06736
Lyubarsky, Y. 2014, MNRAS, 442, L9
Margalit, B., Beniamini, P., Sridhar, N., & Metzger, B. D. 2020, ApJL, 899, L27
Mereghetti, S., Savchenko, V., Ferrigno, C., et al. 2020, ApJL, 898, L29
Metzger, B. D., Margalit, B., & Sironi, L. 2019, MNRAS, 485, 4091
Moore, A. M., & Kasliwal, M. M. 2019, NatAs, 3, 109
Niino, Y., Morokuma, T., Sako, S., et al. 2020, GCN, 27678, 1
Palmer, D. M., & Team, B. A. T. 2020, GCN, 27665, 1
Pen, U.-L., & Connor, L. 2015, ApJ, 807, 179
Petroff, E., Hessels, J. W. T., & Lorimer, D. R. 2019, A&ARv, 27, 4
Rea, N., Testa, V., Israel, G. L., et al. 2004, A&A, 425, L5
Ridnaia, A., Svinkin, D., Frederiks, D., et al. 2020, arXiv:2005.11178
Rieke, G. H., & Lebofsky, M. J. 1985, ApJ, 288, 618
Stamatikos, M., Malesani, D., Page, K. L., & Sakamoto, T. 2014, GCN, 16520, 1
Stefanescu, A., Kanbach, G., Słowikowska, A., et al. 2008, Natur, 455, 503
Sun, X. H., Reich, P., Reich, W., et al. 2011, A&A, 536, A83
Surnis, M. P., Joshi, B. C., Maan, Y., et al. 2016, ApJ, 826, 184
Tam, C. R., Kaspi, V. M., van Kerkwijk, M. H., & Durant, M. 2004, ApJL, 617, L53
Tavani, M., Casentini, C., Ursi, A., et al. 2020, arXiv:2005.12164
The CHIME/FRB Collaboration, Andersen, B. C., Bandura, K. M., et al. 2020, arXiv:2005.10324
Younes, G., Kouveliotou, C., Jaodand, A., et al. 2017, ApJ, 847, 85
Younes, G., Guver, T., Enoto, T., et al. 2020, ATel, 13678, 1
Zackay, B., Ofek, E. O., & Gal-Yam, A. 2016, ApJ, 830, 27
Zhang, C. F., Jiang, J. C., Men, Y. P., et al. 2020, ATel, 13699, 1
Zhong, S. Q., Dai, Z. G., Zhang, H. M., & Deng, C. M. 2020, ApJL, 898, L5
Zhou, P., Zhou, X., Chen, Y., et al. 2020, arXiv:2005.03517